Modeling and Simulation of Anchoring Processes for Small Body Exploration*

Marco B. Quadrelli† Hammad Mazhar, Dan Negrut ‡

This paper describes recent work done in modeling and simulation of anchoring processes in granular media, with applications to anchoring on a Near Earth Object (NEO), where the forces due to interactions with the regolith are much stronger than the local surface gravity field. This effort is part of a larger systems engineering capability developed at JPL to answer key questions, validate requirements, conduct key system and mission trades, and evaluate performance and risk related to NEO operations for any proposed human or robotic missions to a NEO.

Nomenclature

$\nabla\Phi$ Jacobian Matrix
F Force, N
m Mass, kg
Δx Variable displacement vector
α Acceleration, m/s^2
ρ soil density
g local gravity magnitude
p normal pressure
ϕ soil friction angle
m_0 the initial mass of the anchor
σ_c maximum soil compressive stress
$N_{c,g,q}$ soil bearing capacity factors
$s_{c,g,q}$ anchor shape factors
F_c cohesion force
A Hamaker coefficient ($4.3 \times 10^{-20}[J]$)
S is the surface cleanliness parameter, in the range $[0.1, 1]$
Ω $1.5 \times 10^{-10}[m]$
R reduced radius $R = \frac{r_1 r_2}{r_1 + r_2}$
$\mathcal{A}, \mathcal{B}$ bodies in contact
$\mathbf{q}$ generalized coordinates
$\mathbf{r}$ position vector
ϵ quaternion parameter
ω angular velocity
n_i normal at the contact pointing toward the exterior of body
$\mathbf{u_i}, \mathbf{w_i}$ vectors in the contact plane
$\hat{\gamma}_{i,n,u,w}$ contact multipliers
$\mathbf{F_{i,N}}$ normal component of the contact force acting on body $\mathcal{B}$
$\mathbf{F_{i,T}}$ tangential component of the contact force acting on body $\mathcal{B}$
$\mathbf{v_{i,T}}$ relative tangential speed

*Copyright © California Institute of Technology

†corresponding author, marco.b.quadrelli@jpl.nasa.gov, Autonomous Systems Division, Jet Propulsion Laboratory, California Institute of Technology, 4800 Oak Grove Drive, Pasadena, CA 91109

‡Simulation Based Engineering Laboratory, Department of Mechanical Engineering, University of Wisconsin Madison, Madison, WI 53706

$\mu_{i,s}$ static friction coefficient

Subscript

i body index

I. Introduction

NASA is interested in designing a spacecraft capable of visiting a Near Earth Object (NEO), performing experiments, and then returning safely. Certain periods of this mission will require the spacecraft to remain stationary relative to the NEO. Such situations require an anchoring mechanism that is compact, easy to deploy and upon mission completion, easily removed. The design philosophy used in the project relies on the simulation capability of a multibody dynamics physics engine. On Earth it is difficult to create low gravity conditions and testing in low gravity environments, whether artificial or in space is costly and therefore not feasible. Through simulation, gravity can be controlled with great accuracy, making it ideally suited to analyze the problem at hand.

Effective NEO exploration requires vehicle/astronaut anchoring due to extremely low gravity. Simulation and testing must be carried out with implications on system/mission design, system verification and validation, design of combined vehicle/human/robot teams, design of proximity operations such as: landing, tethered operations, surface mobility, drilling, sub-surface sampling. EVA (Extra-vehicular Activity) requires innovative tethering/anchoring techniques for the astronauts to move in the vicinity of a Small Body. In all these cases, a motorized winch network may provide support for astronaut surface operations. A motorized winched network also provides the vertical reaction force needed for drilling and sample collection. Robot arm sampling device interactions with terrain during sample collection also need to be understood. Hopping/crawling robots may interact with regolith material on surface of NEO and can hop at various angles with adjustable strengths to achieve a desired vertical height or horizontal distances. In all these cases, an anchoring process is involved. Anchors may be used as hand or footholds, or possible attach points for ropes that hold an astronaut or equipment to the surface.

In this paper, using an analytical approach to soil interaction and a simulation package capable of utilizing massively parallel GPU hardware (Chrono::Engine[33]), several validation experiments were performed. Ultimately, the outcome of this effort would be an analysis of several different anchor designs, along with a recommendation on which anchor is better suited to the task of anchoring.

In the following, Section II describes the approach considered in this study. Section III discusses aspects of the regolith modeling, and section IV the analytical modeling of the forces acting on a penetrating object. Section V describes the equations of motion of the multibody anchoring system. Section VI discusses the modeling of the inter-body contact and friction forces involved in the simulation of the anchoring process. Section VII summarizes and discusses simulation results, and Section VIII concludes the paper.

II. Description of Approach

To provide context, the study approach is built upon an integrated set of physics-based models as illustrated in Figure 1. The focus of this paper is on the right side of this block diagram. The block diagram shows each element of the integrated model of spacecraft and end-effector dynamics,[6] which includes the models of: the planning function, where the spacecraft trajectory and attitude are specified; the vehicle attitude and orbital dynamics; the vehicle GNC functions, including orbital and attitude estimator and navigation filters; the deployable manipulator dynamics and hinge actuation; the end-effector, anchoring, or in-situ sampling device dynamics and actuation; the Small Body shape, orbital dynamics, and polyhedral gravity models; the communication, power, and lighting geometric analysis; the multi-scale properties of the surface regolith; and the interaction of the end-effector, anchoring, or in-situ sampling device with the surface regolith. The block diagram includes feedback loops to the spacecraft controller from the hinge states of a deployed robotic manipulator, the end effector states, and the amount of mass collected, assuming all these states are known. If not known, they can possibly be estimated. The reason for including these additional functions is that sensing these states are all possibilities in a scenario where an algorithm is needed to monitor the duration of the sample event (dwell time), and a change in each one of these states can be used as a trigger to terminate the event. Previous work which proposes an adaptive capability for surface

sampling is described in,[26].[27] For instance, monitoring the flow of collected mass via a photocell will signal that indeed exogenous matter has entered the spacecraft system, and the event collect sample can now be terminated. A change of relative attitude of the end effector or boom angle (or hinge angle) with respect to the spacecraft attitude (as measured with respect to the surface plane) will indicate that the end effector has indeed contacted the ground.

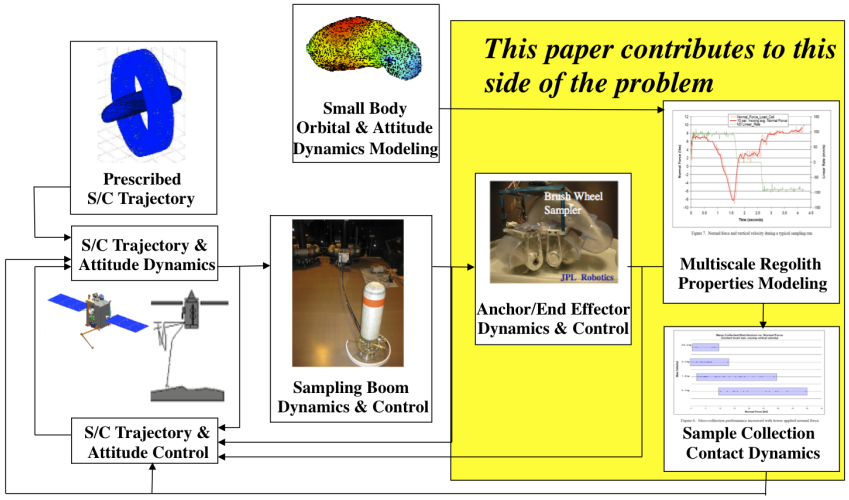

Figure 1. Anchoring GNC block diagram.

An important element in the understanding of the anchoring penetration process is the physics of the regolith, which is described next.

III. Regolith Modeling

Present understanding is that all asteroids that have been observed at close range appear to be covered by meters of strength-less regolith, in which case the anchor pull-out capacity is dependent on the weight of the overlying material. In general, large asteroidal bodies typically spin slowly and may have more strengthless material on the surface than smaller bodies, which tend to spin faster. This understanding implies that, in general, slow anchoring methods such as those based on drilling or melters will require the spacecraft Attitude Control System (ACS) to be involved for vehicle stabilization. Conversely, fast anchoring method such as those based on tethered spikes, telescoping spikes, and multi-legged with tethered or telescoping spikes will likely require less ACS involvement. Early studies on anchoring for the ST4/Champollion mission selected a 1 kg 1.9cm diameter truncated cone penetrator for anchoring onto the surface on materials of strength up to 10 Mpa with a 45 degree impact angle within a reasonable velocity range (100-200 m/s) with a minimum pullout resistance of 450 N in any direction. Several anchoring deployment/retrieval issues must be carefully considered that can impact the mission design. An anchor may ricochet adversely on surface instead of solidly emplacing on ground. Also, drilling a helical anchor requires a torque transfer to another object. PHILAEs landing gear uses ice screws and three landing legs with two pods in each, for example. Harpoons can be easily launched before landing. More than one anchor needs to be deployed from the spacecraft to ensure static stability. Spacecraft ACS (reaction wheels, not RCS) will probably need to be on during the Anchoring Phase to avoid slack cables and vehicle stability problems. Some anchor designs will allow them to be pulled out, others will not.

Behavior of the regolith is likely governed by cohesion and surface adhesion effects that dominate particle interactions at small scales through van der Waals forces. Electrostatic forces are are generally negligible except near terminator crossings where it can lead to significant dust transport. The micro-gravity and solar radiation dominate system behavior prior to soil engagement or penetration. Figure 2 summarizes the essential differences between the environment at a NEO and the environment at the Moon.

Soil mechanics experiments have known issues when it comes to testing samples of regolith in one-g. First, a reproducible preparation of a homogeneous soil sample is difficult to achieve. Second, a characterization of

Phenomena	Moon	NEO
Gravity	Higher order harmonics from mascons (at the milliGal level)	Polyhedral gravity models
Surface Acceleration	Same as gravity acceleration	Order of magnitude variations
Orbital stability	Long term drift due to mascons	Mix of stable and unstable orbit "families"
Target Body Orbital Period	~30 day period	Hours
Porosity	Small	30-50 %
Morphology	Planet-like	Rubble pile
Regolith mechanical properties	Friction dominated – like sand / rocks	Cohesion dominated - like bread flour ?
Interesting surface features	Rocks, craters	Rocks; electro-statically generated dust ponds; large-scale cohesively bound structures

Figure 2. Differences between NEO and Moon.

the soil properties in depth is difficult, since static parameters are typically measured at the surface. Third, under 1-g load, according to soil theory, the compressive strength in depth is significantly influenced by overburden terms, i.e. the effective strength/resistance increase with depth. The soil shear stress can be modeled as

$$\sigma_c = c + p\tan(\phi_f) \tag{1}$$

This is the Mohr-Coulomb limit soil bearing capacity theory, where ϕ_f, is known as the friction angle (or internal-angle-of-friction), p is normal pressure, and the zero normal-stress intercept, c, is known as the cohesion (or cohesive strength, i.e. shear stress at p=0) of the soil. For typical regolith simulant, the cohesion is 40 Pa at loosely packed conditions and increases to 10 kPa at 100 relative density. The friction angle also increases monotonically from 25 deg to 60 deg. The Rosetta Lander design takes advantage of this effect of greatly increased cohesion by local compression of the cometary regolith under the landing pods during landing. Previous relevant regolith modeling work,[7] and[14] covers both low-velocity (approx. 1 m/s) impact of blunt bodies into dust-rich, fluffy cometary materials (Biele et al[7]), as well as high-velocity (approx. 10 m/s) impact of sharp projectiles on various types of soil. (Allen[1] and Anderson et al[3]). The lower limit of the tensile strength is of the order of 1kPa whereas the probable upper limit can be taken as 100kPa. The lower limit of tensile strength corresponds to a compressive strength of c $\geq$ 7kPa. This wide range of soil properties must be capture in simulation, which poses a significant challenge.

At very low gravity and vacuum conditions the biggest unknown is the material strength of the surface material. Neither the Deep Impact mission nor other comet observations have provided firm data on the strength of cometary material. Theoretical considerations and laboratory measurements for weakly bound aggregates and the few observational constraints available for comets and cometary meteoroids lead to estimates of the quasi-static tensile (or shear) strength of cometary material in the dm to m range as of the order of 1kPa, while the compressive strength is estimated to be of the order of 10kPa. In the following, we summarize the current state of knowledge in asteroidal and cometary regolith behavior.

- *Cohesion, tensile, shear and compressive strength*: While for brittle materials tensile strength is generally less than the shear strength, compressive strength is about one order of magnitude higher than tensile strength. In the case of soft landing compressive strength is the relevant parameter. Shear, tensile and compressive strength are indicated by σ_s, σ_t, σ_c, respectively.

- *Dynamic and quasi-static strength*: During impacts, due to very high strain rates, the dynamic strength is typically higher than the quasi-static strength. It is known that the strength increases with strain-

rate resulting in values about an order of magnitude higher (or even more) than the quasi-static strength for the same material. Generally the tensile strength σ_t is proportional to a power b of the strain rate $\dot{\epsilon}$ with a power law exponent typically around 1/4 to 1/3, depending on the material.

- *Size dependence*: Different theories indicate that the strength decreases with increasing size according to d^{-q} where the exponent q is approximately 0.5 (fractal aggregate with fractal dimension D = 2.5 of ice). Thus, if extrapolated from typical lander (0.1m), or impactor (1m) to typical comet (1 to 10 km) scales, the size effect alone would produce a factor of 100 in the apparent strengths. This is in line with the observation that comets can often be described as essentially strength-less bodies (large cometesimal, rubble pile, swarm models) globally, while locally a significant material strength is to be expected.

- *Breakup of Comets, Topography Observations*: Tidal disruption of comets indicate low global tensile strengths in the order of $100 \div 10,000$ Pa. For example, the break-up of Shoemaker-Levy 9 during its perijove in 1992 set a rough upper limit of the tensile strength (on global/km scales!) of 100Pa. The tensile strength of sun-grazing comets has been estimated as 10kPa with some uncertainty due to thermal stresses. Images by Stardust from comet 81P/Wild-2 showed that the cometary surface must have a finite strength on short scales (< 100 m) to support the observed topographic features; because of the small gravity, some 10P a might suffice. Otherwise, only lower bounds on the tensile strengths are available in the order of $1 \ldots 100$ Pa.

- *Breakup of Meteoroids*: Another source of information about possible strength values of cometary surfaces on mm $\div dm$ scales stems from the analysis of meteoroids associated with certain comets which enter the earth atmosphere at high speeds and finally break-up and create a light flash. Wetherill[36] gives values for tensile strengths of these fireballs ranging from 1 kPa to 1 MPa. More recently, Trigo-Rodrguez and Llorca[34] have studied a broad data base of meteor ablation light curves and arrive at tensile strengths between (400 ± 100 Pa and 40 kPa, clustering around 10kP a for not too evolved and rather low density $<$ 1g/cm3 (if known) cometary meteoroids.

- *Laboratory Measurements*: The small scale (cm) shear and tensile strength of snow in the relevant density range of $300 \div 500$ kg/m3 is of the order of $10 \div 100 kPa$. The tensile strength of snow is nearly independent on temperature, while the compressive strength shows a remarkable increase with decreasing temperatures. Simulating possible cometary analogue material in the scope of the KOSI experiments concluded that the small-scale compressive strength of porous mixtures of crystalline ice and dust lies in the range between 30kPa and 1MPa with increasing strength for an increasing dust fraction.

- *Limits Derived from Comet Size and Rotation*: Stability against disruption due to rotation yields lower limits for the combination of bulk density and tensile strength. Rotational periods and sizes for many comets are known, but the corresponding bulk densities are not well constrained. For example, a fast rotating big comet such as C/Hale-Bopp (1995 O1) could be a strength-less rubble pile with a bulk density as low as 100 kg/m3.

- *Theoretical Estimates*: There are different approaches to describe the tensile strength of powders on the basis of van der Waals interactions, cf. Greenberg et al.,[11] or Chokshi et al.[?] The latter model includes the elastic deformation of contacting spherical grains. The theoretical tensile strength of fluffy aggregates depends on particle radii, contact areas, packing geometry and typically scales with the bulk density. Greenberg et al. estimate a tensile strength, for interstellar silicate dust/ice material with a density of 280kg/m3, of 270 Pa. Sirono and Greenberg[29] derive 300 Pa for the tensile and 6000 Pa for the compressive strength for a medium composed of ice grains linked into chains by intermolecular forces. Kuhrt and Keller[16] derive a theoretical strength of 100Pa and 100 kPa for grains of 1mm and $1\mu m$, respectively. Note that 95% of the Deep Impact ejecta dust cross section is represented by particles $r < 1.4\mu m$. From the discussion above the conclusion can be drawn that the cometary surface on meter scales has a reasonable lower limit of the tensile strength of the order of 1kPa whereas the probable upper limit can be taken as 100 kPa.

Next, we discuss approaches to Verification and Validation ($V\&V$) of regolith modeling and simulation. Verification of simulation models is necessary to make sure the correct equations modeling the physics are

correctly implemented in software. Validation of the simulation model with experimental results is also necessary to correctly capture the physics in simulation. While verification can be done at the software level, validation with experiment, especially experiments in micro-gravity, tends to be very costly. Therefore, other approaches for $V\&V$ of microgravity physics models need to be sought. Validation experiments that could be conducted include: a) Photoelastic method, where stress chains are viewed in cross-polarizers;[2] b) Pink plastic beads, where the contact between polystyrene ball and pink translucent plastic sheet is observed;[17] c) Wet beads, where water between glass beads provides cohesive forces; d) Vertical emplacement tests using penetrator shot by gun; e) Vertical soil bearing capacity tests using regolith simulant; and f) Neutral density beads floating in water, coated with vaseline or silicon oil. Known issues with Soil Mechanics Experiments are that reproducible preparation of homogeneous soil sample is notoriously difficult. Furthermore, characterization of soil in depth is difficult, since static parameters are measured at surface.Under 1-g load, according to soil theory, the compressive strength in depth is significantly influenced by overburden terms: effective strength/resistance increase with depth.

Now that the foundations of the regolith behavior have been laid out, in the next section we delve into the analysis of the soil interaction process during penetration.

IV. Modeling of Forces acting on Penetrating Object

A complete and general solution describing the penetration of an anchor or projectile into a solid body is not known, though there are several published models available which may be applicable to the anchor (see, e.g., those listed by Wang[35]). For current modeling efforts we consider the anchor to be a rigid, conically tipped cylindrical projectile, where θ is the half opening angle of the cone.[3] Several possible forces may contribute to the overall deceleration experienced by the projectile during penetration.[1] These may depend on penetrated depth and velocity as well as target material parameters. Most of the forces can be expressed as the integral of decelerating stresses over the wetted surface S_w of the penetrator in contact with the target material. The main force terms of clear (or plausible) physical origin found in the published literature are as follows:

- A constant term associated with compressive strength, possibly including a contribution from the targets self-weight. The latter should be negligible on the comet, where the surface gravity g is expected to be no more than about 1/2000 of that on Earth. It may be more significant for ground-based experiments where the projectile is fired downwards into a cohesion-less target, though the fact that it is also proportional to the diameter of the projectile means that the term is still quite small for laboratory-scale experiments.

- A term which increases linearly with depth due to the weight per unit volume ρg of the overlying material (overburden pressure). As with the self-weight, this should be negligible on the small body but needs to be considered for ground-based experiments, especially those with cohesion-less targets. This term is also proportional to a factor $N_q(\phi)$. For the limit $\phi = 0$, $N_q = 1$ and the term becomes analogous to buoyancy in a fluid.

- A dynamic drag term proportional to the target density ρ and the square of velocity V, resulting from the transfer of momentum from the projectile to the target material. In many cases the importance of drag is incorporated by adopting a drag coefficient C_D (which may itself have a velocity dependence), analogous to the parameter used in fluid dynamics.

- Sliding friction between the projectile surface and the target material, governed by the coefficient of sliding friction μ_f and the total normal stress from the three terms above.

- A viscosity or damping term, proportional to the component of velocity parallel to the projectiles surface. As with friction, this force acts parallel to the anchors surface rather than normal to it. The physical validity of this term seems to be a matter for debate.

- The weight of the projectile. This is only important when significant compared to the other (decelerating forces.

Collecting these terms together with the appropriate geometric factors, one obtains the following equation for the overall deceleration:

$$-\frac{dV}{dt} = \frac{1}{m}\int\int_{S_w}[(\frac{1}{2}C_D\rho V^2\sin^2\theta^{'} + \sigma + \rho g N_q z) \times (\sin\theta^{'} + \mu_f\cos\theta^{'}) + k_v V\cos^2\theta^{'}]dA - g \tag{2}$$

In this equation, $\theta^{'} = \theta$ along the conical tip, but $\theta^{'} = 0$ along the cylindrical shaht of the penetrating object. Also, from Komle,[14] $N_q(\phi) = \exp(\pi\tan\phi)\tan^2(\frac{\pi}{4} + \frac{\phi}{2})$, and k_v is a constact with units of $[Nsm^{-3}]$, i.e., those of viscosity divided by the thickness of a representative boundary layer around the projectile where viscous flow occurs..

From,[14] a parameter analogous to a drag coefficient can be defined in terms of the material parameters as

$$C_D = \frac{2}{(1-\eta)\cos^2\theta} \times [\frac{(1-\eta) + 1/\alpha + \eta/(2-\alpha)}{\eta^{\alpha/2}} - \frac{1}{\alpha} - \frac{1}{2-\alpha}] \tag{3}$$

where $\alpha = 3\lambda/(3+2\lambda)$, $\lambda = \tan(\phi)$, ϕ is the angle of internal friction, $\eta = 1 - \frac{\rho_0}{\rho}$ is the volumetric strain, ρ_0 is the bulk density of the target material before penetration. The case $\eta = 0$ implies zero compression.

After,[14] the compressive stress and the drag term can be combined together, so that the radial pressure exerted on an area element of the target material in contact with an area element of the penetrators surface can be written as:

$$\sigma = [\eta^{-\alpha/2} - 1]\frac{\tau_0}{\lambda} + [\frac{(1-\eta) + 1/\alpha + \eta/(2-\alpha)}{\eta^{\alpha/2}} - \frac{1}{\alpha} - \frac{1}{2-\alpha}]\frac{\rho_0 V^2\tan^2\theta}{(1-\eta)} \tag{4}$$

where τ_0 is the soil cohesion. Note that σ consists of a constant term and a term proportional to the square of velocity, i.e. this model produces neither a term analogous to viscosity nor an overburden pressure term.

The total decelerating force acting on the penetrator consists then of two components. One is the vertical component of the normal stress on the penetrators conical surface, the second being the vertical component of the sliding friction acting tangentially to the projectiles surface. Combining these two components and integrating over the whole wetted surface S_w of the penetrator gives the following expression for the deceleration of the anchor:

$$-\frac{dV}{dt} = \frac{1}{m}\int\int_{S_w}[(\frac{1}{2}C_D\rho V^2\sin^2\theta^{'} + \sigma + \rho g N_q z) \times (\sin\theta^{'} + \mu_f\cos\theta^{'}) + k_v V\cos^2\theta^{'}]dA - g \tag{5}$$

A. Point mass analysis

To get insight into the sensitivity of the system to the various parameters involved, we derived a simple one-dimensional model of the system behavior during penetration. Assumptions used in the derivation of this reduced model are the following. The anchor is modeled as a point-like body with variable mass and area. The mass of body increases because of soil compaction. The soil properties are constant. The gravity level is constant. The soil penetration is modeled following the previous section. The system equations are integrated with a 4-th order constant step Runge-Kutta integrator. Under these assumptions, the final equations of motion of the penetrating anchor become:

$$v = \dot{h} \tag{6}$$

$$\dot{v} = g - \frac{A\sigma_c}{M} - \frac{\rho A C_D v^2}{2M} \tag{7}$$

$$\dot{m} = \rho A v \tag{8}$$

$$M = m_0 + m(t) \tag{9}$$

$$\sigma_c = s_c c N_c + \rho g(\frac{1}{2}s_g A N_g + s_q N_q h) \tag{10}$$

where ρ is the soil density, g is the local gravity level, m_0 is the initial mass of the anchor, σ_c is the maximum soil compressive stress, N_c, N_g, N_q are soil bearing capacity factors, s_c, s_g, s_q are shape factors which depend on the penetrator cross-section shape, and c is the cohesion coefficient.

Figure 3(a) depicts the soil bearing stress factors used in the soil constitutive equation, and figure 3(b) shows the soil bearing stress vs. depth as a function of the soil friction coefficient. As expected, the

penetration is less when the friction coefficient is high. Figure 4 depicts the soil bearing stress vs. depth as a function of (a) friction angle, and (b) gravity level. In these cases, the lower cohesion and lower gravity level would be representative of penetration into a powdery soil, while the higher cohesion levels represent the case of a more compact soil. Figure 5 depicts the soil bearing stress vs. depth as a function of (a) penetrator diameter , and (b) soil density. Figure 5 depicts the soil bearing stress vs. depth as a function of (a) penetrator mass , and (b) cone angle. The last two figures confirm the fact that a larger diameter anchor would penetrate less, and that a heavier anchor would penetrate deeper. All these results assume an initial approach velocity of 1 m/s.

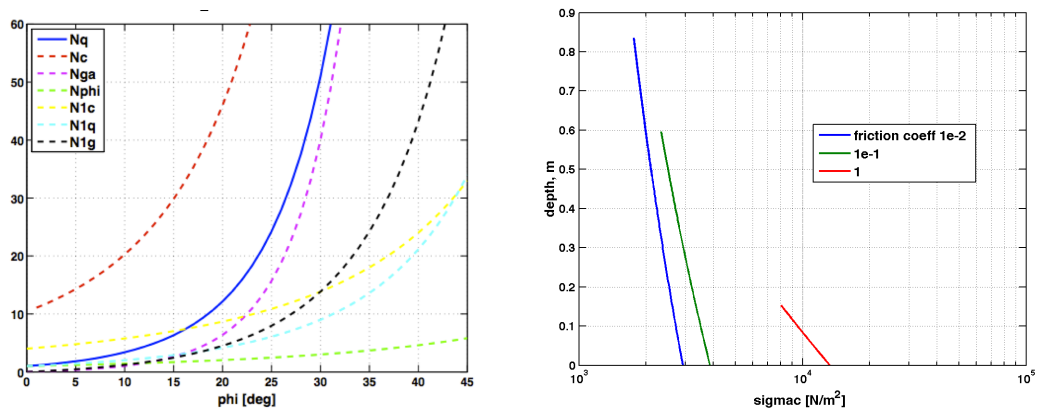

(a) (b)

Figure 3. (a) Soil bearing stress factors, (b) Soil bearing stress vs. depth as a function of friction.

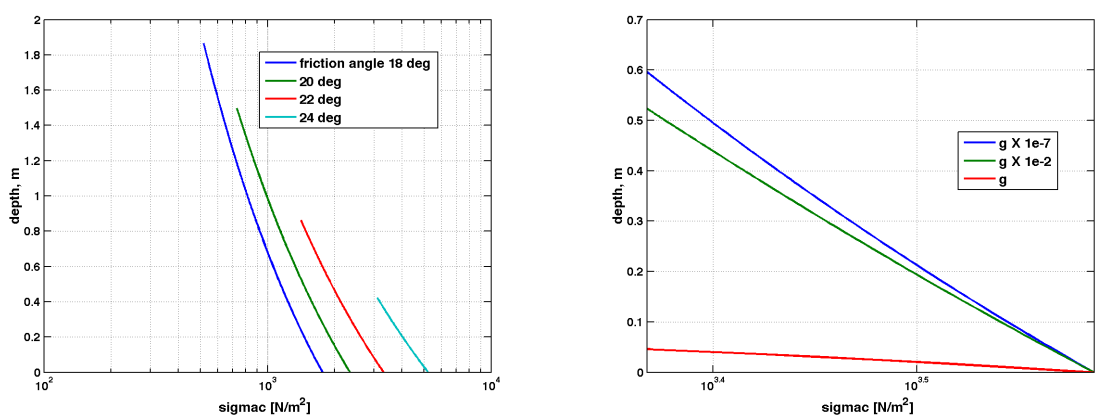

(a) (b)

Figure 4. Soil bearing stress vs. depth as a function of (a) cohesion, and (b) gravity level.

Now that we have insight into the system behavior with a simple model, we increase the fidelity of the model and consider the soil interaction process with a multibody dynamics model. This is done in the next section.

V. Equations of Motion of Multibody Anchoring System

The deployment and retrieval of the end-effector, anchoring, or in-situ sampling device is carried out by means of a multi-link or continuous manipulator. Different sampling arm types that have been considered inclide: a) a rigid, multi-link articulated arm with joint control; b) a flexible deployable, coilable boom

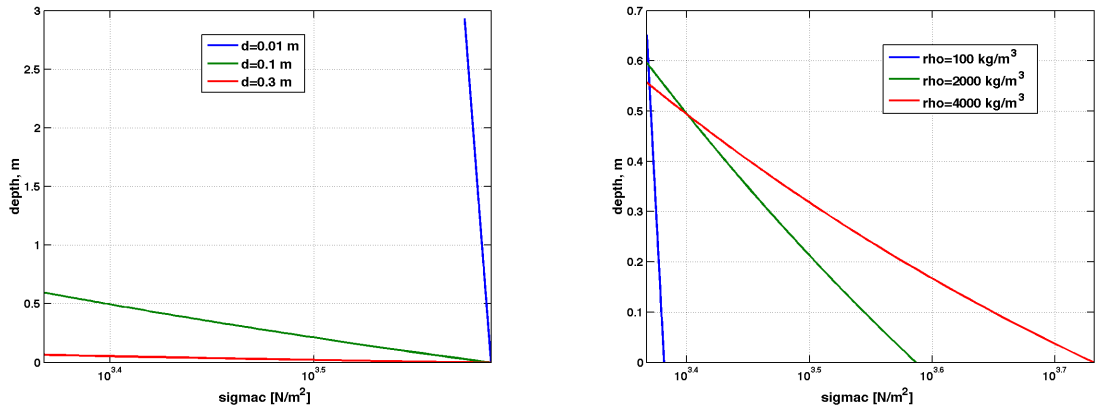

(a) (b)

Figure 5. Soil bearing stress vs. depth as a function of (a) penetrator diameter , and (b) soil density.

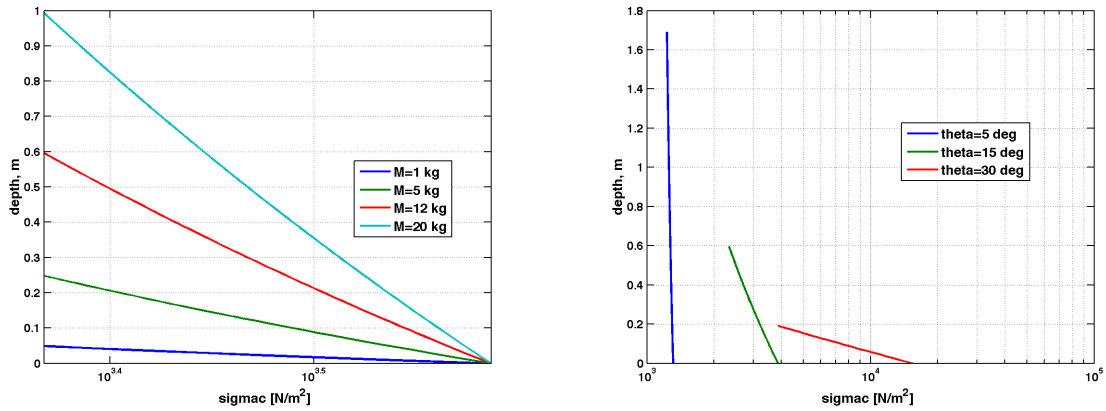

(a) (b)

Figure 6. Soil bearing stress vs. depth as a function of (a) penetrator mass , and (b) cone angle.

with locking joints; c) a deployable truss with joint control; and d) a continuum boom with distributed control. Figure 7 shows the components included in the system level multibody dynamics analysis model of spacecraft, manipulator, and small body.

The simulation of multiple rigid bodies at an extreme scale becomes an increasingly parallelizable problem difficult to run on todays sequential processors in a meaningful amount of time. Until recently,[?] the high cost of parallel computing limited the analysis of such large systems to a small number of research groups. This is rapidly changing, owing in large part to general-purpose computing on the graphics processing unit, or GPU (GP-GPU). GP-GPU computing has been very vigorously promoted by NVIDIA since the release of the CUDA development platform,[21] an application interface for software development targeted to run all NVIDIA GPUs. A large number of scientific applications have been developed using CUDA, most of them dealing with problems that are quite easily parallelizable such as molecular dynamics or signal processing. Very few GP-GPU projects are concerned though with the dynamics of multibody systems, the two most significant being the Havok[13] and the NVIDIA PhysX[25] engines. Both are commercial and proprietary libraries used in the video-game industry and their algorithmic details are not public. Typically, these physics engines trade precision for efficiency as the priority is in speed rather than accuracy. In this context, the goal of our effort was to somewhat de-emphasize the efficiency attribute and instead implement an open source, general-purpose physics-based GPU solver for multibody dynamics backed by convergence

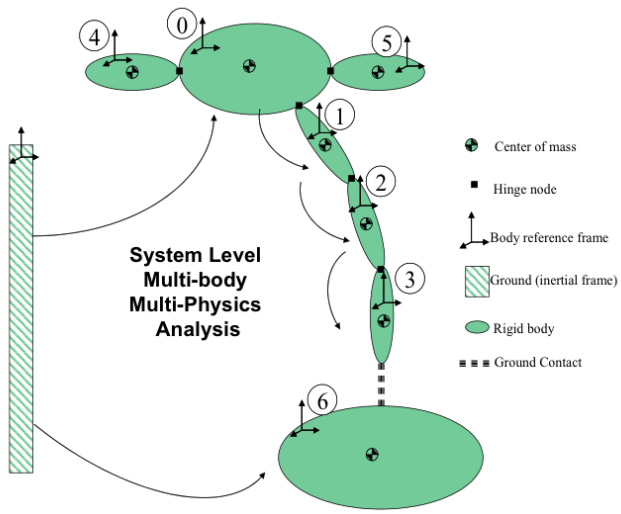

Figure 7. Multibody Dynamics Model of Contact Event.

results that guarantee the accuracy of the numerical solution. Unlike the so-called penalty or regularization methods, where the frictional interaction can be represented by a collection of stiff springs combined with damping elements that act at the interface of the two bodies, the approach embraced here draws on time-stepping procedures producing weak solutions of the differential variational inequality (DVI) problem, which describes the time evolution of rigid bodies with impact, contact, friction, and bilateral constraints. Recent approaches based on time-stepping schemes have included both acceleration-force linear complementarity problem (LCP) approaches[22] and velocity-impulse, LCP-based time-stepping methods.[30–32] The LCPs, obtained as a result of the introduction of inequalities accounting for non-penetration conditions in time-stepping schemes, coupled with a polyhedral approximation of the friction cone, must be solved at each time step in order to determine the system state configuration as well as the Lagrange multipliers representing the reaction forces. If the simulation entails a large number of contacts and rigid bodies, as is the case for granular materials, the computational burden of classical LCP solvers can become significant. Indeed, a well-known class of numerical methods for LCPs based on simplex methods, also known as direct or pivoting methods,[9] may exhibit exponential worst-case complexity. Moreover, the three-dimensional Coulomb friction case leads to a nonlinear complementarity problem (NCP). The use of a polyhedral approximation to transform the NCP into an LCP introduces unwanted anisotropy in friction cones and significantly augments the size of the numerical problem. In order to circumvent the limitations imposed by the use of classical LCP solvers and the limited accuracy associated with polyhedral approximations of the friction cone, a parallel fixed-point iteration method with projection on a convex set has been developed.[5] The method is based on a time-stepping formulation that solves at every step a cone-constrained quadratic optimization problem. The time-stepping scheme has been proved to converge in a measure differential inclusion sense to the solution of the original continuous-time DVI. Using this method a GPU based simulation capability was implemented in the open source Physics Engine: Chrono::Engine,[33].[4]

The state of a mechanical system with n_b rigid bodies in three dimensional space can be represented by the generalized positions $\mathbf{q} = [{r_1}^T, {\epsilon_1}^T, \ldots, {r_{n_b}}^T, {\epsilon_{n_b}}^T]^T \in \mathbb{R}^{7n_b}$ and their time derivatives $\dot{\mathbf{q}}$, where r_i is the absolute position of the center of mass of the $i-th$ body and the quaternion ϵ_i expresses its rotation. One can also introduce the generalized velocities $\mathbf{v} = [{r_1}^T, {\omega_1}^T, \ldots, {r_{n_b}}^T, {\omega_{n_b}}^T]^T \in \mathbb{R}^{7n_b}$, directly related to $\dot{\mathbf{q}}$ by means of the linear mapping $\dot{\mathbf{q}} = \mathbf{L}(\mathbf{q})\mathbf{v}$ that transforms each angular velocity (expressed in the local coordinates of the body) into the corresponding quaternion derivative $\dot{\epsilon}_i$ by means of the linear algebra formula $\dot{\epsilon}_i = \frac{1}{2}G(\epsilon_i)\omega_i$, with[12]

$$G(\epsilon_i) = \begin{bmatrix} +\epsilon_1 & +\epsilon_0 & -\epsilon_3 & +\epsilon_2 \\ +\epsilon_2 & +\epsilon_3 & +\epsilon_0 & -\epsilon_1 \\ +\epsilon_3 & -\epsilon_2 & +\epsilon_1 & +\epsilon_0 \end{bmatrix} \tag{11}$$

Mechanical constraints, such as revolute or prismatic joints, can exist between the parts: they translate into algebraic equations that constrain the relative position of pairs of bodies. Assuming a set of constraints is present in the system, for all $i \in \mathcal{B}$ they lead to the scalar equations $\Psi_i(\mathbf{q}, \mathbf{t}) = \mathbf{0}$. To ensure that constraints are not violated in terms of velocities, one must also satisfy the first derivative of the constraint equations, that is $\nabla {\Psi_i}^T \mathbf{v} + \frac{\partial \mathbf{\Psi_i}}{\partial \mathbf{t}} = \mathbf{0}$ with the Jacobian matrix $\nabla_q \Phi_i = [\partial \Psi_i / \partial \mathbf{q}]^{\mathbf{T}}$ and $\partial {\Phi_i}^T = \nabla_{\mathbf{q}} {\Psi_i}^T \mathbf{L}(\mathbf{q})$. Note that the term $\frac{\partial \Psi_i}{\partial t}$ is zero for all scleronomic constraints, but it might be nonzero for constraints that impose some trajectory or motion law, such as in case of motors and actuators. If contacts between rigid bodies must be taken into consideration, colliding shapes must be defined for each body, and a collision detection algorithm must be used to provide a set of pairs of contact points for bodies whose shapes are near enough, so that a set $\mathcal{A}$ of inequalities can be used to concisely express the non-penetration condition between the volumes of the shapes, i.e. for all $i \in \mathcal{A}$, $\Phi(\mathbf{q}) \geq \mathbf{0}$. Note that for curved convex shapes, such as spheres and ellipsoids, there is a unique pair of contact points, that is the pair of closest points on their surfaces, but in case of faceted or non-convex shapes there might be multiple pairs of contact points, whose definition is not always trivial and whose set may be discontinuous. The model of the inter-body contact and friction forces is discussed in the next section.

VI. Model of inter-body contact and friction

As shown in Figure 8, given two bodies in contact $\mathcal{A}, \mathcal{B}$, let n_i be the normal at the contact pointing toward the exterior of body $\mathcal{A}$, and let $\mathbf{u_i}$ and $\mathbf{w_i}$ be two vectors in the contact plane such that $\mathbf{n_i}, \mathbf{u_i}, \mathbf{w_i} \in \mathbb{R}^{\mathbf{3}}$ are mutually orthogonal vectors: when a contact i is active, that is for $\Phi(\mathbf{q}) = \mathbf{0}$, the frictional contact force act on the system by means of multipliers $\hat{\gamma}_{i,n} \geq 0$, $\hat{\gamma}_{i,u}$, and $\hat{\gamma}_{i,w}$, that is the normal component of the contact force acting on body $\mathcal{B}$ is $\mathbf{F_{i,N}} = \hat{\gamma}_{\mathbf{i,n}} \mathbf{n_i}$ and the tangential component is $\mathbf{F_{i,T}} = \hat{\gamma}_{\mathbf{i,u}} \mathbf{u_i} + \hat{\gamma}_{\mathbf{i,w}} \mathbf{w_i}$ (for body $\mathcal{B}$ these forces have the opposite sign).

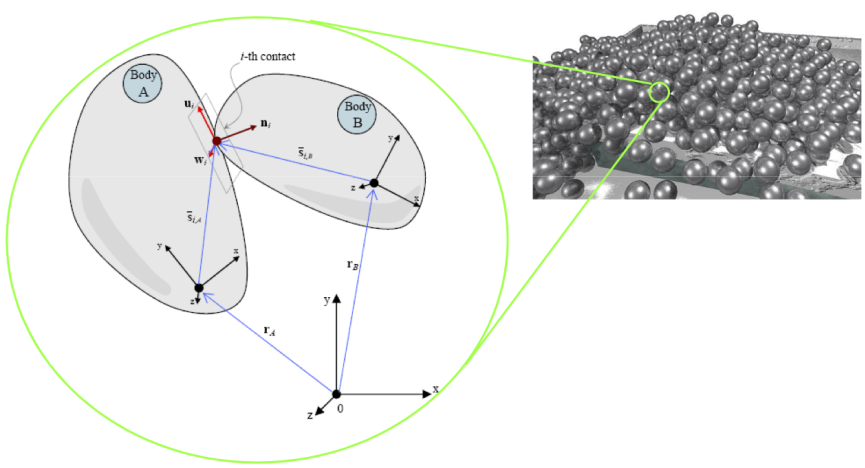

Figure 8. Modeling of contact between two bodies

Also, according to the Coulomb friction model, in case of nonzero relative tangential speed $\mathbf{v_{i,T}}$ the direction of the tangential contact force is aligned with $\mathbf{v_{i,T}}$ and it is proportional to the normal force as $\| \mathbf{F_{i,T}} \| = \mu_{\mathbf{i,d}} \| \mathbf{F_{i,N}} \|$ by means of the dynamic friction coefficient $\mu_{i,d} \in \mathbb{R}^+$. However, in case of null tangential speed, the strength of the tangential force is limited by the inequality $\| \mathbf{F_{i,T}} \| \leq \mu_{\mathbf{i,s}} \| \mathbf{F_{i,N}} \|$ using a static friction coefficient $\mu_{i,s} \in \mathbb{R}^+$., and its direction is one of the infinite tangents to the surface. In our model we assume that $\mu_{i,s}$ and $\mu_{i,d}$have the same value that we will write μ_i for simplicity, so the above mentioned Coulomb model can be stated succinctly as follows:

$$\hat{\gamma}_{i,n} \geq 0, \quad \Phi_i(\mathbf{q}) \geq \mathbf{0}, \quad \mathbf{\Phi_i}(\mathbf{q}) \hat{\gamma}_{\mathbf{i,n}} = \mathbf{0} \tag{12}$$

The first condition states that the friction force is always within the friction cone, i.e.

$$\mu_i \hat{\gamma}_{i,n} \geq \sqrt{\hat{\gamma}_{i,u}^2 + \hat{\gamma}_{i,w}^2} \tag{13}$$

The second condition states that the friction force and the velocity between two contacting bodies are collinear and of opposite direction, i.e.:

$$\langle \mathbf{F_{i,T}}, \mathbf{v_{i,T}} \rangle = - \parallel \mathbf{F_{i,T}} \parallel \parallel \mathbf{v_{i,T}} \parallel \tag{14}$$

The third condition, which captures the stick-slip transition, is:

$$\parallel \mathbf{v_{i,T}} \parallel (\mu_\mathbf{i} \hat{\gamma}_\mathbf{i,n} - \sqrt{\hat{\gamma}^\mathbf{2}_\mathbf{i,u} + \hat{\gamma}^\mathbf{2}_\mathbf{i,w}}) \tag{15}$$

Note that the condition $\hat{\gamma}_{i,n} \geq 0, \quad \Phi_i(\mathbf{q}) \geq \mathbf{0}, \quad \mathbf{\Phi_i}(\mathbf{q})\hat{\gamma}_\mathbf{i,n} = \mathbf{0}$ can be also written as a complementarity constraint: $\hat{\gamma}_{i,n} \geq 0, \quad \Phi_i(\mathbf{q}) \geq \mathbf{0}$, see (Stewart and Trinkle[32]). This model can also be interpreted as the Karush-Kuhn-Tucker first order conditions of an equivalent maximum dissipation principle (Moreau[19]), which can be written as:

$$i \in \mathcal{A}: \quad \hat{\gamma}_{i,n} \geq 0, \perp \Phi_i(\mathbf{q}) \geq \mathbf{0}, \quad , (\hat{\gamma}_\mathbf{i,u}, \hat{\gamma}_\mathbf{i,w}) \underset{\mu_\mathbf{i}\hat{\gamma}_\mathbf{i,n} \geq \sqrt{\hat{\gamma}^\mathbf{2}_\mathbf{i,u} + \hat{\gamma}^\mathbf{2}_\mathbf{i,w}}}{\mathbf{argmin}} \mathbf{v^T}(\hat{\gamma}_\mathbf{i,u}\mathbf{D_{i,u}} + \hat{\gamma}_\mathbf{i,w}\mathbf{D_{i,w}})) \tag{16}$$

Finally, we must also consider the effect of external forces with the vector of generalized forces $\mathbf{f}(\mathbf{t}, \mathbf{q}, \mathbf{v}) \in \mathbb{R}^{\mathbf{6n_b}}$, that might contain gyroscopic terms, gravitational effects, forces exerted by springs or dampers, torques applied by motors, and so on. Considering the effects of both the set $\mathcal{A}$ of frictional contacts and the set $\mathcal{B}$ of bilateral constraints, the system cannot be reduced neither to an ordinary differential equation (ODE) of the type $\dot{v} = \mathbf{f}(\mathbf{t}, \mathbf{q}, \mathbf{v})$ nor to a differential-algebraic equation (DAE), because of the inequalities and because of the complementarity constraints, that rather turn the system into a differential inclusion of the type $\dot{v} \in \mathcal{F}(\sqcup, \mathbf{q}, \mathbf{v})$, where $\mathcal{F}$ is a set-valued multifunction (Pfeiffer, Foerg et al.[?]). In fact, the time evolution of the dynamical system is governed by the following differential variational inequality (DVI):

$$\begin{cases} \dot{\mathbf{q}} = \mathbf{L}(\mathbf{q})\mathbf{v} \\ \mathbf{M}\dot{\mathbf{v}} = \mathbf{f}(\mathbf{t}, \mathbf{q}, \mathbf{v}) + \sum_{\mathbf{i} \in \mathcal{B}} \hat{\gamma}_\mathbf{i,n} \nabla \mathbf{\Psi_i} + \sum_{\mathbf{i} \in \mathcal{A}} (\hat{\gamma}_\mathbf{i,n}\mathbf{D_{i,n}} + \hat{\gamma}_\mathbf{i,u}\mathbf{D_{i,u}} + \hat{\gamma}_\mathbf{i,w}\mathbf{D_{i,w}})) \\ i \in \mathcal{B}: \quad \Psi_i(\mathbf{q}, \mathbf{t}) = \mathbf{0} \\ i \in \mathcal{A}: \quad \hat{\gamma}_{i,n} \geq 0, \perp \Phi_i(\mathbf{q}) \geq \mathbf{0}, \quad , (\hat{\gamma}_\mathbf{i,u}, \hat{\gamma}_\mathbf{i,w}) \underset{\mu_\mathbf{i}\hat{\gamma}_\mathbf{i,n} \geq \sqrt{\hat{\gamma}^\mathbf{2}_\mathbf{i,u} + \hat{\gamma}^\mathbf{2}_\mathbf{i,w}}}{\mathbf{argmin}} \mathbf{v^T}(\hat{\gamma}_\mathbf{i,u}\mathbf{D_{i,u}} + \hat{\gamma}_\mathbf{i,w}\mathbf{D_{i,w}})) \end{cases} \tag{17}$$

Here, to express the contact forces in generalized coordinates, we used the tangent space generators $D_i = [\mathbf{D_{i,n}}, \mathbf{D_i u}, \mathbf{D_{i,w}}] \in \mathbb{R}^{\mathbf{6n_b} \times \mathbf{3}}$ that are sparse and are defined given a pair of contacting bodies A and B as:

$$D_i{}^T = \begin{bmatrix} \mathbf{0} & \dots & -A_{i,p}{}^T & +A_{i,p}{}^T A_A \tilde{\bar{\mathbf{s}}}_\mathbf{i,A} & \mathbf{0} & \dots \\ \mathbf{0} & \dots & +A_{i,p}{}^T & -A_{i,p}{}^T A_B \tilde{\bar{\mathbf{s}}}_\mathbf{i,B} & \mathbf{0} & \dots \end{bmatrix} \tag{18}$$

where we use $A_{i,p} = [\mathbf{u_i}, \mathbf{v_i}, \mathbf{w_i}]$ as the $\mathbb{R}^{3\times3}$ matrix of the local coordinates of the i-th contact, and introduce the vectors $\bar{s}_{i,A}$ and $\bar{s}_{i,B}$ to represent the positions of the contact points expressed in body coordinates. A superscript tilde denotes a skew-symmetric operator. The DVI in (2) can be solved by time-stepping methods: in detail, the discretization requires the solution of a complementarity problem at each time step, and it has been demonstrated that it converges to the solution to the original differential inclusion for $h \to 0$ (Stewart and Trinkle;[32] Stewart[31]). Moreover, the differential inclusion can be solved in terms of vector measures: forces can be impulsive and velocities can have discontinuities, thus supporting also the case of impacts and giving a weak solution to otherwise unsolvable situations like in the Painlev paradox (Stewart[30]).

In addition to the contact and friction forces, short range cohesion forces also play a role, and this is discussed in the next section.

A. Modeling of Short Range Interaction Forces

In low gravity environments, gravitational forces become less prevalent in comparison to cohesive and electrostatic forces. Figure 9,[28] shows that as the gravitational force decreases, the radius at which the attractive forces between particles of lunar regolith become equivalent to gravitational forces increases as gravity decreases. In order to simulate the effects of short range forces, the simulation capability was augmented with support for an additional contact based force system. Unlike frictional forces, which act at the surface of

an object, interaction forces such as cohesion can apply within a certain boundary around an object. This interaction distance acts as the cutoff for the force. When there is contact between the two boundaries, a force is applied to both objects, when they separate the force becomes zero. Short range interaction forces are modeled using a fixed boundary/envelope around each collision geometry. Figure 10 shows envelopes around a sphere and a box. An additional collision detection phase is performed using the envelopes rather than the actual collision geometry. This collision detection phase yields a list of intersections that are then processed in parallel; each contact gets an associated force. It is possible for objects to have multiple forces from multiple envelope intersections. A reduction step is performed to compute the resultant force and apply it to each object. For Lunar Regolith, cohesion operates on separation distances of $(10)^{(} - 10)$ meters, this distance relates to the surface cleanliness of the regolith.[23] Surface cleanliness,$S = 1.5(10)^{(} - 10)/t$, where t is the separation distance, is a measure of how close particles can get to each other. For example on earth, due to water molecules and gases in the atmosphere, the surface cleanliness is close to 0.1, on the side of the Moon facing the Sun, however, the surface cleanliness is close to unity. Because the amount of molecules and gases that are deposited on the free surface of the regolith is small, the van der Waals force between regolith particles is large. This force is given by $F_c = \frac{AS^2R}{48\Omega^2}$ and can be simplified to $F_c = 3.6 \times 10^{-2}S^2R$ [9], where A is the Hamaker coefficient $(4.3 \times 10^{-20}[J])$, S is the surface cleanliness parameter, in the range $[0.1, 1]$, $\Omega = 1.5 \times 10^{-10}[m]$, and R is the reduced radius $R = \frac{r_1 r_2}{r_1 + r_2}$.

Gravity [Gs]	Grain Radius [m]	Analog body
1	$6.5\ x\ 10^{-4}$	Earth
.1	$2\ x\ 10^{-3}$	Moon
.01	$6.5\ x\ 10^{-3}$	Vesta (180 km)
.001	$2\ x\ 10^{-2}$	Eros (10km)
.0001	$6.5\ x\ 10^{-2}$	Toutatis (1.8 km)
.00001	$2\ x\ 10^{-1}$	Itokawa (.18) km
.000001	$6.5\ x\ 10^{-1}$	(.018 km)
.0000001	$2\ x\ 10^{-0}$	KW4 Equator

Figure 9. Assuming Lunar Regolith, this table shows the radius at which weight and cohesion forces become equivalent, along with parent body sizes.

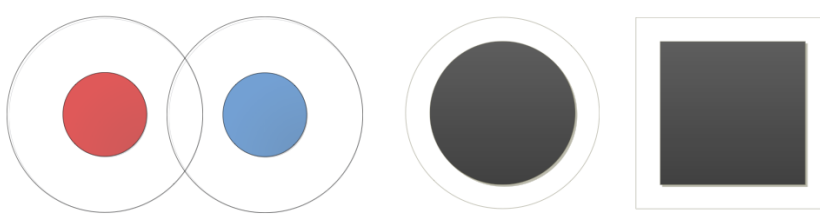

Figure 10. Bounding Boxes for short range interaction force conputation and collision detection

Next, the settling behavior is investigated.

B. Settling Behavior

In order to capture short range interaction forces properly, it is important that the granular material not interpenetrate. There are several ways to reduce the amount of interpenetration: Reduce time step, increase the number of the linear complementarity problem (LCP) iterations, and increase the responsiveness of each LCP iteration. To better understand the behavior of the parallel LCP solver a parametric study was performed using these three parameters.

The parameters in Figure 11 were used to run 180 different simulations consisting of a long slender box in which 10 spheres were dropped. The width of the box was slightly larger than the width of the sphere, keeping the spheres stacked on top of each other. Each simulation was run for 5 seconds and the kinetic

energy was measured for the entire system. If the rate at which the kinetic energy decreases is higher, the system reaches a state of rest faster with less interpenetration. When the energy is low but hasnt reached zero, it means that objects are still moving and slowly sinking into one another. Figure 12(a) shows the results for a simulation with 100 LCP iterations and a .1 scaling factor. When comparing to Figure 12(b), which is 1000 iterations with a .1 scaling factor, the rate at which the kinetic energy decreases to zero is much greater. It is possible to converge to a stable configuration faster with less iterations if the LCP scaling factor is higher, see Figure 12(b), where the scaling factor is 0.8. However, this causes the solver to become unstable when large penetrations do occur as it corrects for them faster, causing large changes in velocity. When velocities become too large, problems with tunneling (objects passing through one another) can occur, further destabilizing the simulation.

CCP Iterations	100	200	400	600	800	1000
Iteration Scaling factor	0.1	0.2	0.4	0.6	0.8	1.0
Timestep [s]	0.005	0.0025	0.001	0.0005	0.00025	

Figure 11. Parameters used in Cone Complementarity study to capture interaction forces properly

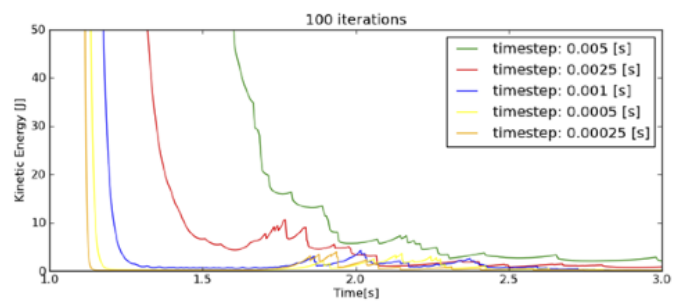

(a)

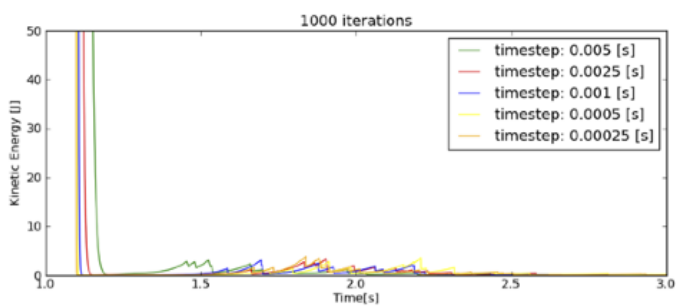

(b)

Figure 12. (a) Simulation with a LCP scaling factor of 0.1 and 100 LCP iterations, (b) Simulation with a LCP scaling factor of 0.1 and 1000 LCP iterations.

VII. Simulation Results

In this section, we discuss the results of numerical experiments done on representative systems (Brazil Nut, Ball Drop) and the final anchoring penetration simulation.

A. Brazil Nut Test

A simulation of the Brazil nut experiment,[15] was completed based on parameters from.[?] Figure 13 show several snapshots of a GPU-driven multibody dynamics simulation of the Brazil nut segregation problem, which was conducted to verify the granular media physics modeling engine. If granular material of two different sizes and densities is placed in the same container and the container is excited with a specific sinusoidal motion, the two materials can be separated with great control. This segregation process is used widely in manufacturing and is a heavily documented phenomenon. Macro level effects have been confirmed; see Figure 13, where the white sphere moves upwards due to the vibration of the container at 30 Hz.

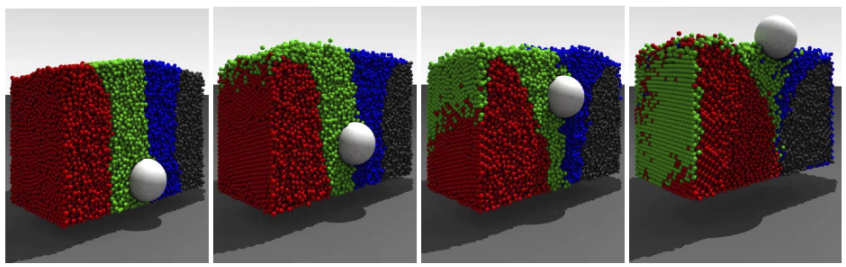

Figure 13. Snapshots of Brazil Nut experiment

B. Ball Drop Experiment

This experiment involves a bed of granular material and a relatively large heavy ball (or impactor) falling into that material.[10] The acceleration profiles of the ball are measured as it is dropped onto the granular material. To simulate the ball drop test, an initial set of test data was created. 250,000 equally sized particles were dropped into a box and allowed to come to a stable state of compaction. This set of data was saved and is reused for each parametric test where the impactor parameters are varied. For tests where the particle parameters are varied, different initial data sets were created. For every combination of impactor and particle type, the position, acceleration, and velocity profiles of the impactor were saved. These profiles were used to make comparisons against experimental data provided in.[10] Currently, particles with a radius of .0035 meters have been simulated for each impactor. Results showed, when compared to literature, that the acceleration caused by the impact was too great and the depth of impactor penetration was too low. The next step is to determine the cause of the inconsistency. Parameters such as the friction coefficient of the walls or the surface of the impactor could be contributing factors to the differences seen.

C. Anchoring Experiments

Unlike the previous experiment, where the motion of the anchor was controlled at the velocity level, in this experiment the motion of the anchor was constrained and forces were applied to move the anchor. Four parameters were modified for this experiment resulting in 10 separate tests. The angle of the anchor, torque applied to the anchor, penetration force, and pullout force of the anchor varied. A listing of these parameters can be seen in Figure 14.

A simulation setup similar to the previous experiment was used, with a few differences. First, the container enclosing the particles was rectangular rather than square to accommodate anchors at shallow angles. Second, the number of particles was greater than before, 32000 rather than 20000, and finally the time step used for this simulation was .0002 [s] rather than .0005[s] resulting in a more accurate simulation. The anchor was pushed into the granular material for two seconds, with the torque being gradually applied once it was in contact with the granular material at 0.1 [s]. Then the anchor was allowed to rest for one second after which it was pulled up for one second. This resulted in a 4 second simulation.

Using the initial test data created for the parametric ball drop test, helical anchors penetrate and anchor into a bed of granular material. Currently, the simulation uses an anchor with a mass of 1 kg which is inserted with a vertical force of 10 N and an axial torque of 10 N-m. Once the anchor penetrates and digs into the material, it is pulled out with a force of 20 N-m. The purpose of this experiment is to set the

Figure 14. Parameters of Helical Anchor experiment

Angle [Deg]	Torque [Nm]	Force Penetration [N]	Force Pullout [N]	h : .0002 [s]
0	2	10	20	G: -9.80665 [m/s^2]
30	2	10	20	Beads: 32000
45	2	10	20	Bead Mass: 2.802 E-04 [kg]
60	2	10	20	Bead Radius: .0035 [m]
0	1	10	20	Bead Density: 1560 [kg/m^3]
0	4	10	20	μ_{bead}: .4245
0	2	0	20	$\mu_{container}$: .5
0	2	20	20	Anchor Mass: .04823 [kg]
0	2	10	10	-
0	2	10	30	-

underlying framework required to test anchors penetrating at different angles, masses, velocities and torques. The force/torque required to remove the anchor from the granular material is measured to determine the effect of different granular materials on the performance of the anchor.

Initially a triangular mesh was to be used for the anchor geometry. This method did not perform well due to the number and size of the triangles in the mesh, which increased the total number of contacts. Therefore, a different approach that involves using geometric primitives was explored. In this approach the anchor is modeled using boxes, cylinders, and spheres. Using primitives rather than a triangulated mesh allows the anchor to be parameterized easily.

A simulation of a helical anchor, penetrating a bed of granular material can be seen in Figure 15. In this simulation, an initial bed of granular material was simulated until the kinetic energy of the system was almost zero. Once this bed was created an anchor was dropped spinning at a constant rate of π radians per second. After three seconds the anchor was pulled out of the bed at a constant velocity until it was completely free.

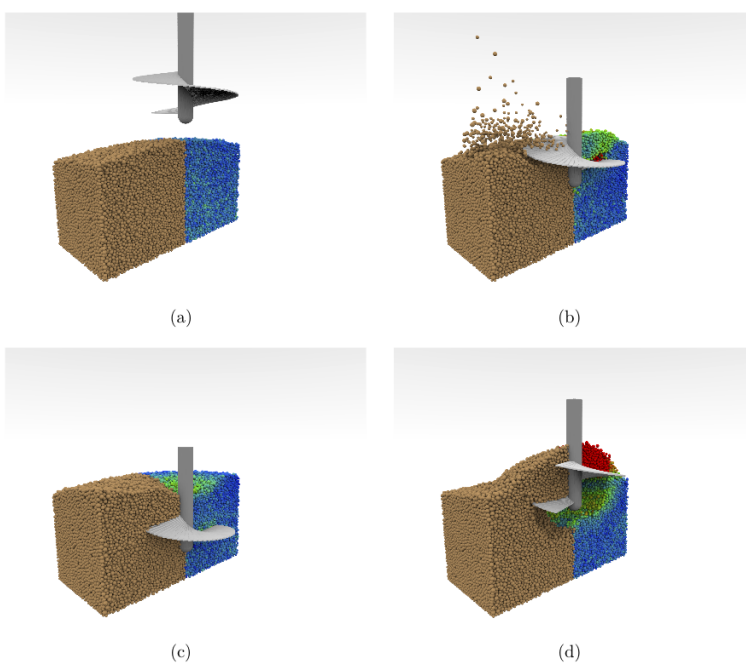

Figure 15. Stages of anchoring, first anchor drops onto granular bed (a), then an applied torque anchors the anchor (b,c), after which it is pulled out (d).

Figure 16 summarizes the results of the simulations. In Figure 16(a) an anchor with different applied torques and a constant pullout force of 300N is simulated, while in Figure 16(b) an anchor with different

pullout forces and a constant torque of 1000N is simulated.

These figures show that if the penetration force is higher, the depth of penetration will be greater. The amount of torque has a smaller effect on the depth that the anchor reaches. However if the torque is too high, in this case 4 [N-m] the anchor begins to rotate too quickly causing cavitation within the granular material. This instability causes the anchor to move erratically within the granular material, reducing the overall effectiveness of the anchor. Based on the results of the increased penetration force, a higher penetration force will allow for better anchoring. A real world example would be screwing a screw into a piece of wood: if no pressure is applied the screw will not anchor into the wood as readily as it would when it is both pushed and rotated. The penetration force has the largest effect in relation to how quickly the anchor penetrated the granular material. Increasing the torque has a much smaller effect. As the penetration angle is reduced from 0 degrees, a vertical anchor, to 90 degrees, a horizontal anchor, the velocity and accelerations experienced by the anchor become smaller. This is because the anchor gradually enters the granular material rather than being forced. Using a shallow angle might be preferred to reduce the overall forces experienced by the anchor. Also it should be noted that the 60 degree anchor anchored just as deep as anchors that were more vertical so the penetration depth was not adversely affected. There is a critical force at which the anchor can be pulled out of the granular material effectively. When the force is too low, in this case 10 [N], it essentially negates gravity causing it to move upwards very slowly. With a force of 20 [N] the anchor is pulled out at a faster rate. There are several improvements that can be made to the simulation experiment. First is that the granular bed be deeper and the container longer. By making the bed deeper it would prevent the anchor from touching the bottom of the container, which occurred in several of the simulations performed. Also with a penetration angle of 60 degrees the anchor is likelier to touch one of the two sides of the container; making the container longer would solve this. In relation to the pullout force several simulations became unstable when the force was applied. This is due to the instantaneous upwards force that was applied; if the force were to be gradually applied it would prevent instabilities and allow the anchor to be pulled out.

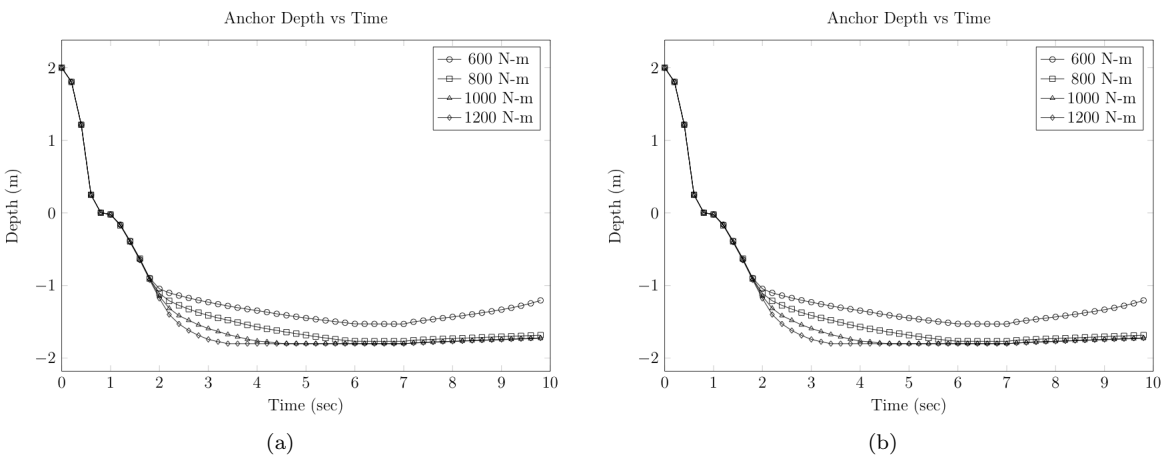

Figure 16. (a) Anchor with different applied torques and a constant pullout force of 300N, (b) Anchor with different pullout forces and a constant torque of 1000N.

VIII. Conclusions

In this paper, using an analytical approach to soil interaction and a simulation package capable of utilizing massively parallel GPU hardware, several validation of anchor penetration experiments were performed. Ultimately, the outcome of this effort would be an analysis of several different anchor designs, along with a recommendation on which anchor is better suited to the task of anchoring. Simulating cohesion accurately is an important step in capturing rigid body dynamics in a NEO low gravity environment. One of the largest factors that control the accuracy of the cohesion model is the stability of the LCP solver and the speed at which it converges to a solution. It is possible to control the convergence rate and interpenetration by stiffening the entire system. Unfortunately, this has the adverse effect of decreasing the stability of the LCP solver. It is possible to increase stiffness without decreasing the stability of the solver, by a combination of

increasing the number of LCP iterations, increasing the LCP scaling factor and decreasing the time step. The short range force model has also been considered in the simulation capability. Macro level validation was carried out with the Brazil Nut and the Ball Drop simulations, where the behavior was observed to be similar to what was expected. Further experiments would include measuring the overall contact force on the anchor to determine how much resistance is applied by the granular media, changing the gravity and anchoring into a bed of varying particle sizes and shapes. Once the cohesion model has been completed and tested, zero gravity tests would then be performed.

Acknowledgement The research described in this paper was carried out at the Jet Propulsion Laboratory, California Institute of Technology, under a contract with the National Aeronautics and Space Administration. H. Mazhar and Dan Negrut were partially supported through Jet Propulsion Laboratory sub-contract 1435056 *Verification and Validation of Granular Media Simulation Capability*. The authors would like to acknowledge the support of Brian Wilcox and Bob Balaram, Abhi Jain, and Hari Nayar of the JPL DARTS Laboratory. The authors would also like to thank the Simulation Based Engineering Laboratory, run by Prof. Dan Negrut, at the University of Wisconsin Madison for support on this project. Thanks also to Partha Shakkotai and Taylor Medford, for assistance with the anchoring modeling and simulation effort.

References

[1]Allen, W.A., Mayfield, E.B., Morrison, H.L., "Dynamics of a projectile penetrating sand". J. Appl. Phys. 28 (3), 1957, 370376.

[2]Allersma, H.G.B., 1987. Optical analysis of stress and strain in photoelastic particle assemblies. PhD Thesis, Delft University of Technology.

[3]Anderson, W.W., Ahrens, T.J., Gibson, A., Scott, R., Suzuki, K., "Emplacement of penetrators into planetary surfaces". J. Geophys. Res. 101 (E9), 21,1996, 13721,149.

[4]M. Anitescu, F. A. Potra, and D. Stewart, Time-stepping for three-dimensional rigid-body dynamics, Computer Methods in Applied Mechanics and Engineering, no. 177, pp. 183197, 1999.

[5]M. Anitescu and A. Tasora, An iterative approach for cone complementarity problems for nonsmooth dynamics, Computational Optimization and Applications, 2008.

[6]Balaram et al., "Physics-Based Simulator for NEO Exploration Analysis and Modeling ", presented at AIAA SPACE 2011 Conference and Exposition, Long Beach, California, Sep. 27-29, 2011.

[7]Biele et al., The putative mechanical strength of comet surface material applied to landing on a comet, Acta Astronautica 65 (2009) 11681178.

[8]A. Chokshi, G.G.M. Tielens, et al., Dust coagulation, Astrophys. J. Pt. I 407 (2) (1993) 806819.

[9]R. W. Cottle and G. B. Dantzig, Complementary pivot theory of mathematical programming, Linear Algebra and Its Applications, vol. 1, pp. 103125, 1968.

[10]D. I. Goldman, Scaling and dynamics of sphere and disk impact into granular media, Physical Review E, vol. 77, no. 2, pp. 1-14, Feb. 2008.

[11]J.M. Greenberg, H. Mizutani, T. Yamamoto, A new derivation of the tensile strength of cometary nuclei: application to Comet ShoemakerLevy 9, Astron. Astrophys. 295 (1995) L35L38.

[12]Haug, E.J.: *Computer-Aided Kinematics and Dynamics of Mechanical Systems, Volume I: Basic Methods*, Allyn and Bacon, Needham Heights, Massachusetts, 1989.

[13]Havok, Havok Physics, 2011. [Online]. Available: http://www.havok.com/.

[14]N.I. Komle et al., Impact penetrometry on a comet nucleus interpretation of laboratory data using penetration models, Planetary and Space Science 49 (2001) 575598.

[15]A. Kudrolli, Size separation in vibrated granular matter, Reports on Progress in Physics, vol. 67, no. 3, pp. 209-247, Mar. 2004.

[16]E. Khrt, H.U. Keller, The formation of cometary surface crusts, Icarus 109 (1994) 121132.

[17]Liu, C.-H.; Nagel, S. R.; Schecter, D. A.; Coppersmith, S. N.; Majumdar, S.; Narayan, O.; Witten, T. A., Force Fluctuations in Bead Packs, Science, Volume 269, Issue 5223, pp. 513-515.

[18]M. MacGregor, Cracking the brazil nut effect, in Colorado State Science Fair, Inc., 1996, pp. 1-20.

[19]Moreau, J. "Unilateral contact and dry friction in finite freedom dynamics." Nonsmooth mechanics and Applications: 1-82, 1988.

[20]Negrut, D., A. Tasora, et al. "Leveraging parallel computing in multibody dynamics." Multibody System Dynamics: 1-23, 2011.

[21]NVIDIA Corporation, Compute Unified Device Architecture (CUDA), 2011. [Online]. Available: http://www.nvidia.com/.

[22]J.-S. Pang and J. C. Trinkle, Complementarity formulations and existence of solutions of dynamic multi-rigid-body contact problems with Coulomb friction, Math. Program, no. 73(2), pp. 199226, 1996.

[23]H. A. Perko, Effects of surface cleanliness on lunar regolith mechanics.pdf, in Proceedings of the Annual Meeting of the American Institute of Astronautics and Aeronautics, 1996.

[24]Pfeiffer, F., M. Foerg, et al. "Numerical aspects of non-smooth multibody dynamics." Computer Methods in Applied Mechanics and Engineering 195(50-51): 6891-6908, 2006.

[25]NVIDIA Corporation, PhysX, 2011. [Online]. Available: http://developer.nvidia.com/technologies/physx.

[26]Quadrelli, B.M., Backes, P., Wilkie, W.K., Keim, J., Quijano, U., Mukherjee, R., Scharf, D., Bradford, S.C., McKee, M.: Investigation of Phase Transition-Based Tethered Systems for Small Body Sample Capture, Acta Astronautica, 68, (2011), 947-973.

[27]Quadrelli, B.M., Backes, P., Wilkie, W. K., Giersch, L., Quijano,: Deployable Tethered Systems for Planetary Sample Capture, presented at the AIAA SPACE 2009 Conference and Exposition, Pasadena, California, 14-17 September 2009.

[28]D. J. Scheeres, C. M. Hartzell, P. Sanchez, and M. Swift, Scaling forces to asteroid surfaces: The role of cohesion, p. 54, Feb. 2010.

[29]S.-I. Sirono, J.M. Greenberg, Do cometesimal collisions lead to bound rubble piles or to aggregates held together by gravity?, Icarus 145 (2000) 230238.

[30]Stewart, D.: "Convergence of a Time Stepping Scheme for Rigid Body Dynamics and Resolution of Painlev's Problem." Archive for Rational Mechanics and Analysis 145(3): 215-260, 1998.

[31]Stewart, D. E.: "Rigid-body dynamics with friction and impact." SIAM Review 42(1): 3-39, 2000.

[32]Stewart, D. E. and J. C. Trinkle: "An implicit time-stepping scheme for rigid- body dynamics with inelastic collisions and Coulomb friction." International Journal for Numerical Methods in Engineering 39: 2673-2691, 1006.

[33]A. Tasora, Chrono::Engine Multibody Dynamics Engine, 2011. [Online]. Available: http://www.chronoengine.info/chronoengine/.

[34]J.M. Trigo-Rodrguez, J. Llorca, The strength of Cometary meteoroids: clues to the structure and evolution of comets, Mon. Not. R. Astron. Soc. 372 (2006) 655660 erratum (375 (2006) 415415).

[35]Wang, W.L.: "Low velocity projectile penetration". J. Soil Mech. Found. Div. Proc. Am. Soc. Civ. Engrs 97 (SM12), 1971, 16351655.

[36]G.W. Wetherill, D.O. Revelle, Relationships between comets, large meteors, and meteorites, in: Comets, University of Arizona, Tucson, AZ, 1982, pp. 297319.